

## Propagation of bird vocalizations in the Alpine environment

Didier DRAGNA<sup>(1)</sup> \*, Loïc BERGER<sup>(1)</sup>, Sébastien OLLIVIER<sup>(2)</sup>, Frédéric SEBE<sup>(3)</sup>

<sup>(1)</sup>Univ Lyon, Ecole Centrale de Lyon, INSA Lyon, Université Claude Bernard Lyon I, CNRS, LMFA, UMR 5509,  
36 Avenue Guy de Collongue, F-69134, ECULLY, France

<sup>(2)</sup>Univ Lyon, Université Claude Bernard Lyon I, Ecole Centrale de Lyon, INSA Lyon, CNRS, LMFA, UMR 5509,  
43 boulevard du 11 novembre 1918, F-69100, VILLEURBANNE, France

<sup>(3)</sup>Univ Lyon, Université Jean Monnet, CNRS, ENES/Neuro-PSI, UMR 9197,  
23 rue Michelon, F-42023, SAINT-ETIENNE, France

### Abstract

Rock ptarmigan is a bird living in the mountains tops, whose population tends to decrease in Europe over the last decade, notably due to climate change, habitat loss and human disturbance. Censusing of number of birds in the Alps is realized via point-count monitoring using birds vocalization. However, detection of bird vocalizations by the human hear is somewhat tricky in these non-homogeneous landforms, due to sound propagation effects. In order to improve the counting method, it is necessary to understand how bird vocalizations propagate in the Alpine environment. With this aim, a propagation model based on a ray-tracing approach is developed and includes topography, ground reflection and absorption and atmospheric refraction and absorption. The model is first validated in both frequency and time domains against reference results obtained with a numerical solution of the linearized Euler equations for simple cases. Propagation of the bird vocalization in the Alpine environment is then illustrated. It is shown that the active space of the bird dramatically depends on the environment. The modeling of active and detection space will provide precise information for the birds monitoring, enabling managers to define more precisely their counting plans.

Keywords: Ethology, Outdoor propagation, Ray tracing

## 1 INTRODUCTION

The rock ptarmigan is a bird (see Fig. 1 (a)) living in the northern parts of Eurasia and North America. In France, it can be found in subalpine and alpine habitats of the Pyrenees and the Alps at altitude greater than 1800 m [1]. Its characteristic vocalization consists of a train of pulses, with frequency content between 900 Hz and 3700 Hz see (Fig. 1 (b)-(c)). Due to climate change and habitat transformation, its population is decreasing. Rock ptarmigan is often considered as a bioindicator, meaning that its population is a global indicator of the biodiversity in alpine environments.

While acoustic monitoring starts to be used [2], the current counting method is based on a human-based approach. The counting area is covered by several observers, spaced apart each other by 500 m, which corresponds to an empirical distance at which rock ptarmigan can not be heard anymore. This protocol has several biases; a single individual can be counted multiple times or can not be detected at all. Indeed, propagation of the bird vocalization in Alpine environment is not simple to due to a complex landform (topography, ground effect) and meteorological conditions. In order to improve current counting methods, it is therefore required to better understand and predict propagation in this environment.

The objective of this paper is to develop a propagation model, suited for the Alpine environment. The paper is organized as follows. In Sec. 2, possible approaches to predict sound propagation are examined and motivations for the use of geometrical methods are discussed. The ray-tracing approach is described. Test-cases to validate

\*corresponding author, didier.dragna@ec-lyon.fr

the numerical model are performed. Application of the model for propagation of rock ptarmigan vocalization in a mountain environment is illustrated in Sec. 3.

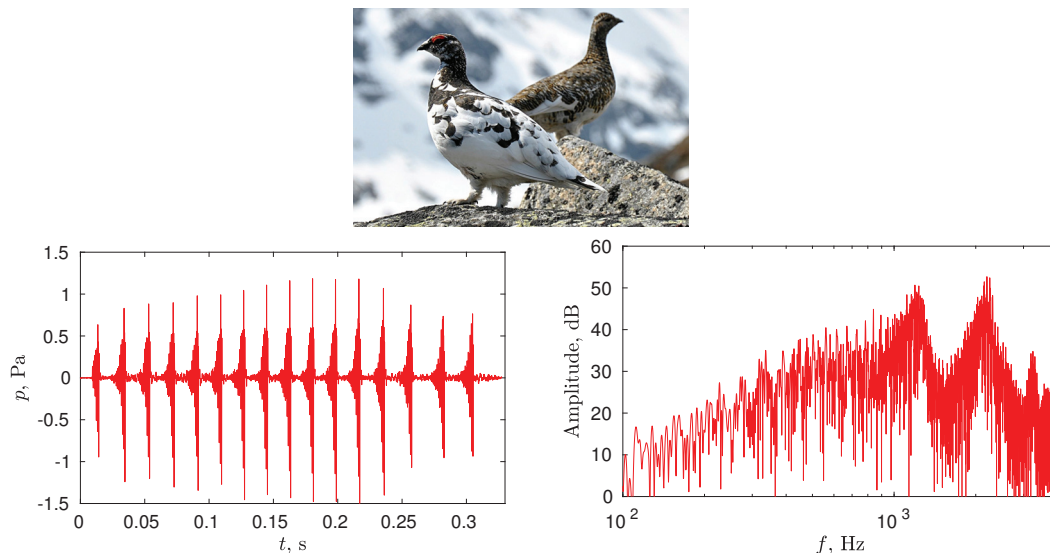


Figure 1. (top) A pair of rock ptarmigans in spring. [3] (bottom) Vocalization of the rock ptarmigan: (left) waveforms and (right) spectrum.

## 2 RAY-TRACING APPROACH

### 2.1 MOTIVATION

There are several ways to predict sound propagation outdoors. Analytical approaches are the fastest ones to obtain reliable results. Standards to compute noise maps are thus based on these approaches. A lot of commercial softwares are available for this purpose. They often take as input data GIS (geographic information system) files, which allow one to account easily for complex landforms. Typical calculation times for an area of several square kilometers is only of a few minutes. There are however two main drawbacks for the use of these softwares in a bioacoustic context. First, the standards implemented in these softwares are developed for octave or one-third octave frequency bands, which does not make it possible to obtain the bird vocalization after propagation. Second, the formulas employed in these standards are often derived from empirical considerations, especially for ground reflection and refraction by the atmosphere. In addition, they were mostly developed for urban environment and their validity for mountain environment is not clear. Note that there has been recently a sound propagation model [4] for anthropogenic noise in wildland environment that has been implemented in the ArcGIS platform. Numerical approaches are also numerous. Wave-based methods are appealing as they can account accurately for most of the phenomena encountered in atmospheric acoustics. Their computational cost however remains prohibitive for large 3D domains. Geometrical methods are an interesting compromise between accuracy and efficiency. They are based on a high-frequency assumption, or more precisely on the assumption that the characteristic length scale of variations of the ambient variables is large compared to the wavelength. They can handle specular reflection on an irregular terrain and refraction by inhomogeneities of the atmosphere. Accounting for diffraction or diffuse reflection is possible, but is usually not included because it significantly complicates the approach. There are however considerable limits to ray-tracing. There are thus two particular regions in which predictions given by the ray-tracing approach are expected to be erroneous. First ones are shadow zones, which are the regions in which no ray penetrates and are due to atmospheric refraction or topography. Geometrical approaches would thus predict a null amplitude for the acoustic field. This is

of importance in Alpine environment, for which terrain irregularities can induce large shadow zones near the ground. The other critical region are caustics, which are points or surfaces on which the cross-sectional area of the ray tube tends to zero. On caustics, the ray-tracing approach predicts an infinite amplitude.

## 2.2 DESCRIPTION

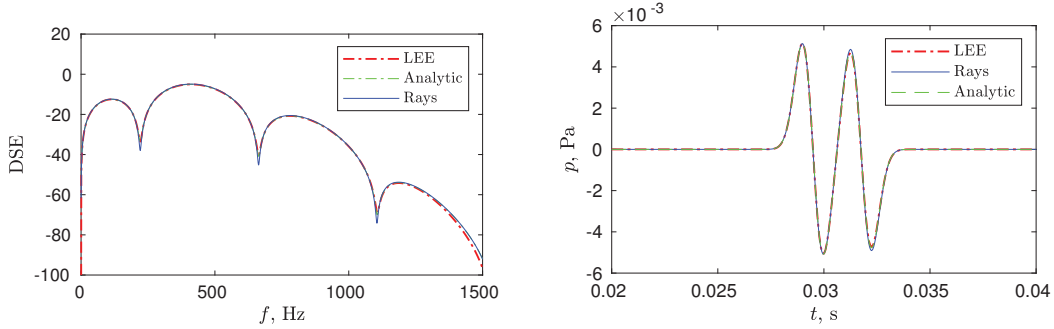


Figure 2. (top) Energy spectral densities and (bottom) time-domain signatures for a source at (0, 0, 1 m) and a receiver at (300 m, 0, 3 m) and for a homogeneous atmosphere.

In the ray-tracing approach [5], the acoustic pressure is sought as  $\hat{p}(f, \mathbf{x}) = A(f, \mathbf{x})e^{i\omega\tau(\mathbf{x})}$ , with  $A$  the amplitude of the pressure which is assumed to be slowly varying and  $\tau$  the travel time. In an inhomogeneous atmosphere at rest with sound speed profile  $\bar{c}(\mathbf{x})$  and density profile  $\bar{\rho}(\mathbf{x})$ , the ray equations are given by:

$$\frac{d\mathbf{x}}{dt} = \bar{c}\mathbf{n} \quad (1)$$

$$\frac{d\mathbf{n}}{dt} = (\mathbf{n} \cdot \nabla \bar{c})\mathbf{n} - \nabla \bar{c} \quad (2)$$

with  $\mathbf{n}$  the unit vector tangent to the ray. From an acoustic point of view, a bird can be considered as a point source, generating a spherical wavefront. The rays are therefore parametrized with two angles  $\varphi$  and  $\theta$ , corresponding to the elevation and azimuthal angles, respectively. Introducing the geodesic elements  $r_\varphi = d\mathbf{x}/d\varphi$  and  $r_\theta = d\mathbf{x}/d\theta$  as well as the variables  $q_\varphi = d\mathbf{n}/d\varphi$  and  $q_\theta = d\mathbf{n}/d\theta$ , it can be shown from Eqs. (1) and (2) that they satisfy the equations:

$$\frac{d\mathbf{r}_\varphi}{dt} = (\mathbf{r}_\varphi \cdot \nabla \bar{c})\mathbf{n} + \bar{c}\mathbf{q}_\varphi \quad (3)$$

$$\frac{d\mathbf{r}_\theta}{dt} = (\mathbf{r}_\theta \cdot \nabla \bar{c})\mathbf{n} + \bar{c}\mathbf{q}_\theta \quad (4)$$

$$\frac{d\mathbf{q}_\varphi}{dt} = (\mathbf{n} \cdot \nabla \bar{c})\mathbf{q}_\varphi + (\mathbf{q}_\varphi \cdot \nabla \bar{c})\mathbf{n} - \mathbf{v}_\varphi + (\mathbf{n} \cdot \mathbf{v}_\varphi)\mathbf{n} \quad (5)$$

$$\frac{d\mathbf{q}_\theta}{dt} = (\mathbf{n} \cdot \nabla \bar{c})\mathbf{q}_\theta + (\mathbf{q}_\theta \cdot \nabla \bar{c})\mathbf{n} - \mathbf{v}_\theta + (\mathbf{n} \cdot \mathbf{v}_\theta)\mathbf{n} \quad (6)$$

with  $\mathbf{v}_\varphi = (\mathbf{r}_\varphi \cdot \nabla)\nabla \bar{c}$  and  $\mathbf{v}_\theta = (\mathbf{r}_\theta \cdot \nabla)\nabla \bar{c}$ . The cross-sectional area of the elementary ray tube along the ray can then be obtained with  $S(t) = |\mathbf{r}_\varphi \times \mathbf{r}_\theta|$ . The amplitude of the pressure along a ray is determined with the Blokhintsev invariant, which states that  $A^2(t)S(t)/(\bar{\rho}(t)\bar{c}(t))$  is constant along a ray tube. The constant is usually obtained by comparing the solution of the ray equations with that of the Helmholtz equation for a homogeneous unbounded medium [6]. For a point source, the amplitude of the pressure is  $A = \hat{s}(f)/r$ , with  $r$  the distance and  $\hat{s}(f)$  is the source strength. Finally, the amplitude of the pressure along a ray is given by:

$$A(t) = \hat{s}(f) \left( \frac{\cos \varphi_s \bar{\rho}(t)\bar{c}(t)}{S(t) \bar{\rho}_s \bar{c}_s} \right)^{1/2} \quad (7)$$

where  $\varphi_s$  is the elevation angle at launch and  $\bar{\rho}_s$  and  $\bar{c}_s$  are the density and sound speed at the source. The parameter  $\hat{s}(f)$  can also be interpreted as the acoustic pressure at 1 m from the source and can account for a possible source directivity. The pressure at an observer is therefore the sum of the contribution of all the rays that reach the observer, which are referred to as eigenrays. Accounting for phase shifts at caustics and possible ground reflections, it can be written as:

$$\hat{p}(f) = \sum_i A_i(t_i) e^{i\omega t_i} = \sum_i \hat{s}(f) e^{i\omega t_i} \left( \frac{\cos \varphi_{s,i} \bar{\rho}(t_i) \bar{c}(t_i)}{S(t_i) \bar{\rho}_s \bar{c}_s} \right)^{1/2} (-i)^{n(i)} \prod_j R_{ij} \quad (8)$$

where  $n(i)$  is the number of times that the eigenray  $i$  has crossed a caustic and  $R_{ij}$  is the reflection coefficient associated to the  $j$ -th reflection of the eigenray  $i$ .

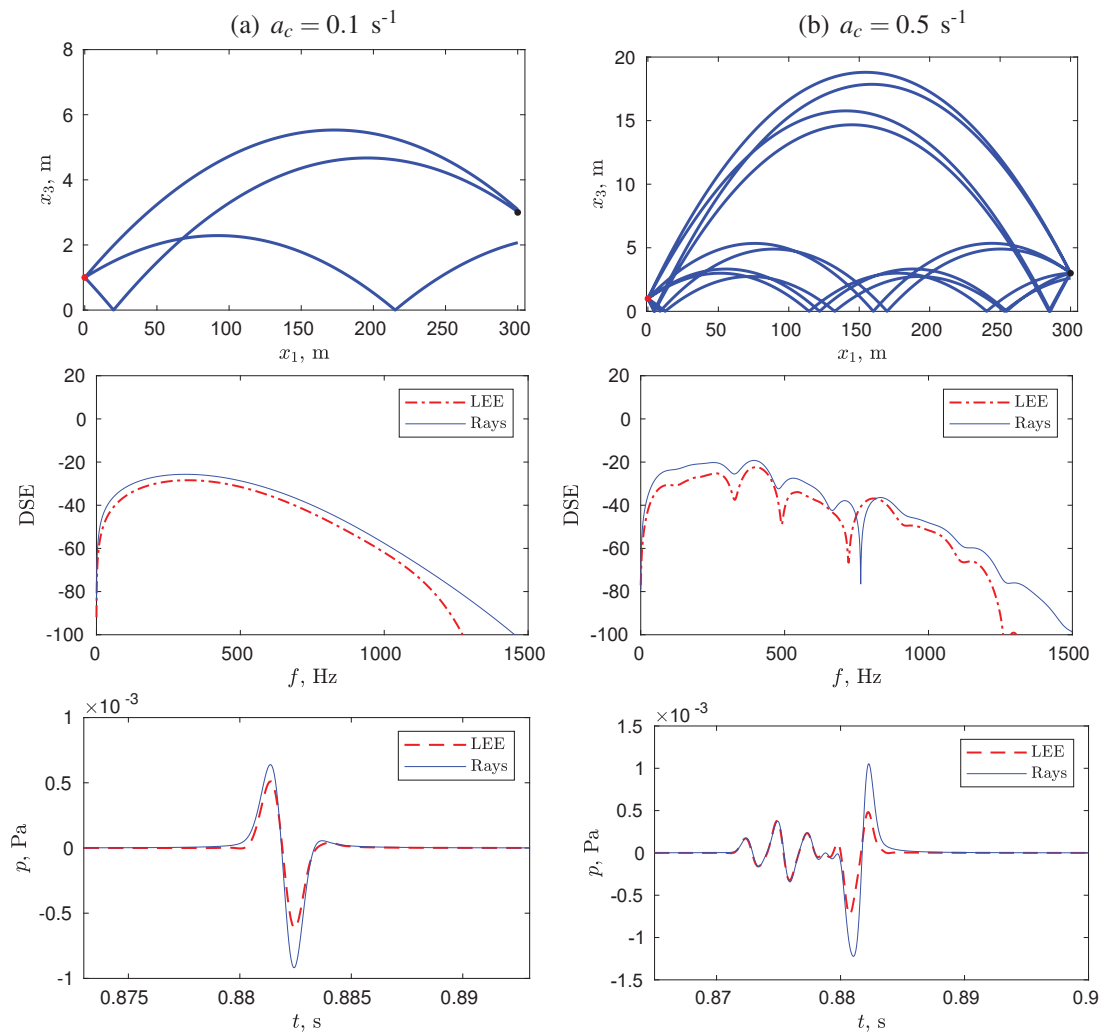


Figure 3. (top) Eigenrays, (middle) energy spectral densities and (bottom) time-domain signatures for a source at (0, 0, 1 m) and a receiver at (300 m, 0, 0.3 m). The sound speed gradient is set to (left)  $a_c = 0.1 \text{ s}^{-1}$  and (right)  $a_c = 0.5 \text{ s}^{-1}$ .

The computation of the sound pressure with the ray-tracing approach is performed in two steps. First, the eigenrays at each receiver are determined. Second, the amplitude along the eigenrays is computed and the

pressure at the receiver is determined with Eq. (8). The first step is by far the more computationally intensive. In particular, the search of eigenrays is somewhat tricky, especially in a large 3D domain. In this study, we use a brute force approach. The launch angles are discretized on a grid  $\varphi \in [\varphi_{\min}; \varphi_{\max}]$  and  $\theta \in [0; 2\pi]$ , with corresponding grid size  $\Delta\varphi$  and  $\Delta\theta$ . For each set of launch angles  $(\varphi, \theta)$ , the ray trajectory is obtained by integrating Eqs. (1) and (2), with a Runge-Kutta algorithm. The minimal distance between the ray and the receiver  $d_{\min}(\varphi, \theta)$  is then determined. After having computed all the ray trajectories, the eigenrays are detected by computing the minima of the function of two variables  $d_{\min}$  and by checking that for each local minimum, the minimum distance to the ray is smaller than a threshold, set to 1 m. Once the eigenrays have been obtained, Eqs. (3)-(6) for the geodesic elements are integrated and the amplitude of the pressure along the ray is determined with Eq. (7). The pressure in the frequency domain at the receiver is finally obtained by summing coherently the contributions of the eigenrays with Eq. (8). The pressure in the time domain can then be computed by calculating the inverse Fourier transform.

The angular steps  $\Delta\varphi$  and  $\Delta\theta$  must be sufficiently small. Indeed, at long range, the launch angles of eigenrays can be very close, in particular in a downward-refracting atmosphere (see, e.g., [7]). Therefore, a large number of rays has to be launched to determine all the eigenrays. For the simulations performed in Sec. 3, approximately  $10^7$  rays were launched. The code is written in MATLAB and is run on a standard workstation.

### 2.3 VALIDATION

In order to validate the ray-tracing approach, comparisons with a numerical solution of the linearized Euler equations (LEE) by a finite-difference time-domain approach [8] are performed. For this, we consider sound propagation above a flat rigid ground in an atmosphere whose sound speed profile varies as:  $\bar{c} = c_0 + a_c x_3$ , with  $c_0 = 340 \text{ m s}^{-1}$ . The density is constant with  $\bar{\rho} = \rho_0 = 1.22 \text{ kg m}^{-3}$ . The source is located at  $(0, 0, 1 \text{ m})$  and generates a short pulse.

In the first test-case, the atmosphere is homogeneous with  $a_c = 0$ . The rays are straight lines and there are only two rays, corresponding to the direct and reflected contributions. Fig. 2 shows the energy spectral densities (ESD) obtained with the ray-tracing approach from Eq. (8) and the corresponding time-domain signals calculated by an inverse Fourier transform. Analytical solution and the numerical solution of the LEE are also shown for comparison. It can be seen that the three solutions perfectly agree in both frequency and time-domain.

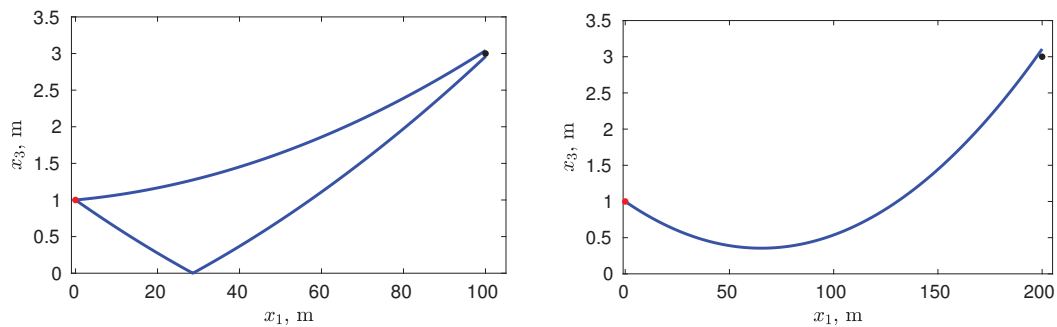


Figure 4. Eigenrays for a source at  $(0, 0, 1 \text{ m})$  and a receiver at [left]  $(100 \text{ m}, 0, 3 \text{ m})$  and [right]  $(200 \text{ m}, 0, 3 \text{ m})$ . The sound speed gradient is set to  $a_c = -0.1 \text{ s}^{-1}$ .

A downward-refracting atmosphere with  $a_c > 0$  is now considered. The eigenrays for a receiver at  $(300 \text{ m}, 0, 3 \text{ m})$ , as well as the ESD and the time-domain signal at the receiver are shown in Fig. 3 for sound speed gradients equal to  $a_c = 0.1 \text{ s}$  and  $a_c = 0.5 \text{ s}$ . For  $a_c = 0.1 \text{ s}$ , an additional eigenray is observed, compared to a homogeneous atmosphere. The ESD is slightly overestimated with reference to the LEE solution by approximately 3 dB over the whole frequency range. A single contribution is seen on the time-domain signal, as the arrival times of the eigenrays are very close. For  $a_c = 0.5 \text{ s}$ , there are 9 eigenrays detected by the algorithm.

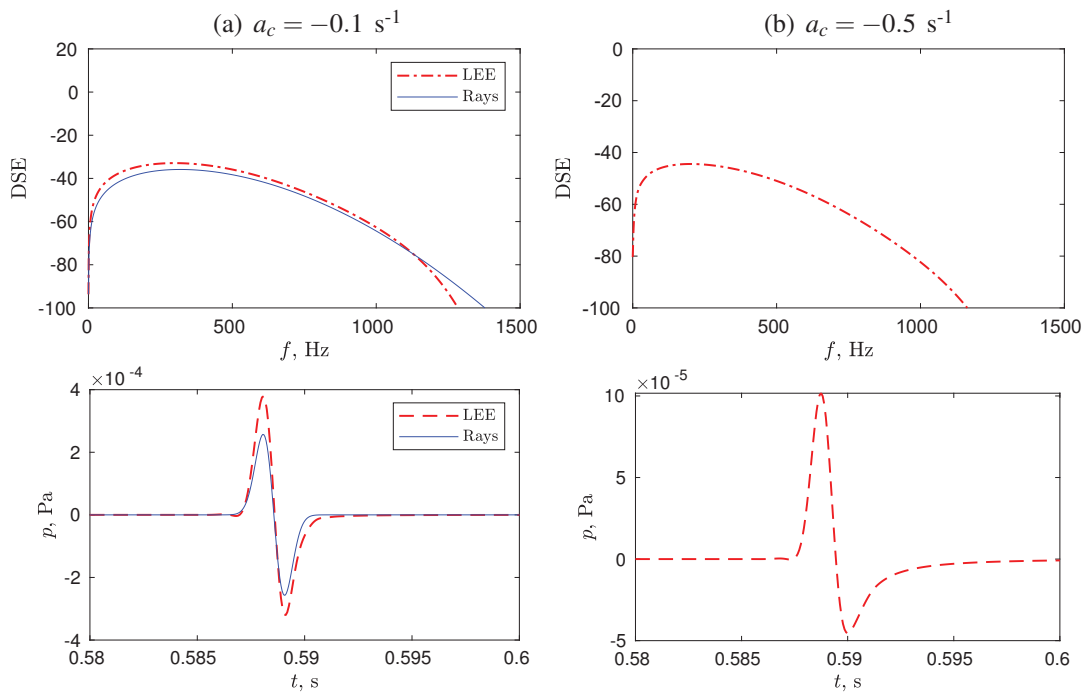


Figure 5. (top) Energy spectral densities and (bottom) time-domain signatures for a source at (0, 0, 1 m) and a receiver at (200 m, 0, 3 m). The sound speed gradient is set to (left)  $a_c = -0.1 \text{ s}^{-1}$  and (right)  $a_c = -0.5 \text{ s}^{-1}$ .

The ESD obtained with the ray-tracing is similar to that of the LEE solution below 600 Hz and above 900 Hz despite an overestimation of a few dB. The destructive interference pattern at a frequency of 800 Hz is also shifted towards a lower frequency. A good agreement is also observed in the time-domain signals. In particular, the three first contributions before  $t < 0.88 \text{ s}$  perfectly superimpose. The amplitude of the last contribution with an arrive time of  $t = 0.88 \text{ s}$  is largely overpredicted. Analysis of the raytube cross-sectional area (not shown here) reveals that the two eigenrays with the longest arrival time are close to a caustic. The evaluation of their amplitude is therefore inaccurate.

In the last case, an upward-refracting atmosphere with  $a_c < 0$  is examined. Eigenrays for receivers at (100 m, 0, 3 m) and (200 m, 0, 3 m) are plotted in Fig. 4. Close to the source, there are still two eigenrays. At larger distances, a single eigenray corresponding to the direct contribution remains, while at even larger distances there is no eigenray at all. Fig. 5 shows the ESD and the time signals predicted at (200 m, 0, 3 m) for sound speed gradients of  $-0.1 \text{ s}^{-1}$  and  $-0.5 \text{ s}^{-1}$ . For  $a_c = -0.1 \text{ s}^{-1}$ , the ray-tracing approach gives only one contribution (see Fig. 4). The ESD and the time signal are in good agreement with those of the LEE solution. For  $a_c = -0.5 \text{ s}^{-1}$ , the receiver is in the shadow zone. Geometrical acoustics then leads to a null pressure. Actually, compared to the case  $a_c = -0.1 \text{ s}^{-1}$ , the amplitude of the pressure signal is reduced by a factor 4, corresponding to a 12 dB reduction.

### 3 PROPAGATION IN THE ALPINE ENVIRONMENT

Results obtained with the ray-tracing approach on the Flaine area are illustrated. Fig. 6 shows the topography of the Flaine area that has been obtained from GIS tools. It is observed that on this area of a few square kilometers, the difference in altitude is about 800 m. A valley can also be seen at  $x_1 = 3.5 \text{ km}$ . It can therefore be expected that sound propagation would be totally different depending on the source location.

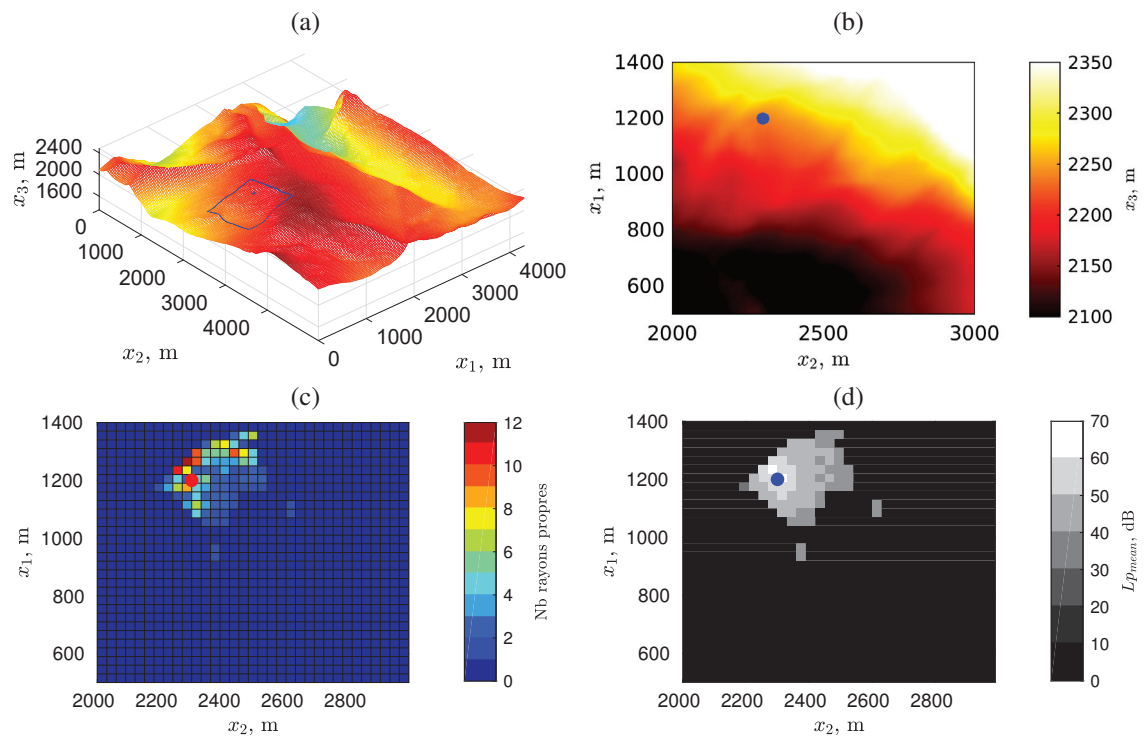


Figure 6. (a) Relief map of the Flaine area and (b) zoom on the are of interest. (c) Number of eigenrays received at each receiver on the map. (d) Map of the sound presure level (SPL).

In this illustration, the source is located at  $x_1 = 1.2$  km and  $x_2 = 2.3$  km and its height is 1 m above the ground. Its location is represented by a dot in Fig. 6. The calculation domain is limited to the blue rectangle in Fig. 6 (a). A zoom on the relief map restricted to the calculation domain is shown in Fig. 6 (b). The terrain slope is largely varying. Near the source, it is almost constant, while for  $x_1 \leq 1$  km the slope is more pronounced. At top right corner of the domain, the terrain is almost flat. Finally, near the source, three small elongated hills oriented along the  $x_1$ -axis can be distinguished. Two of them are located 50 m on the left of the source in Fig. 6 (b). The third one is located at  $x_2 = 2.6$  km on the right of the source.

Receivers are placed on the computational domain at a height of 1.5 m and are spaced regularly, separated by 30 m. The atmosphere is inhomogeneous. The sound speed is varying linearly with the altitude. The sound speed gradient is  $0.2 \text{ s}^{-1}$  and the reference temperature is  $5 \text{ }^\circ\text{C}$  at  $x_3 = 2350$  m. An impedance model of a freshly fallen snow has been used for ground reflection. Fig 6 (c) indicates the number of eigenrays at each receiver. It is significant at the left and at the top of the source, with a maximum number equal to 12. There is no eigenray behind the two small hills at the left of the source. In addition, the third hill prevents ray propagation to the right of the source. The decrease of the slope induces a shadow zone at the receivers located at the top of the domain. Similarly, an other shadow zone is generated due to the increase of the slope for the receivers at the bottom of the domain. There are therefore only few receivers, for which the ray-tracing algorithm gives information on the sound pressure. The corresponding SPL map is shown in Fig 6 (d). It gives information on what is referred to as the active space which is the area around the bird where its vocalization can be detected. It is seen that the topography has a large influence on the SPL. In particular, the SPL does not depend only on the distance from the source. The higher SPL is obtained in the region at the left and at the top of the source for which the number of eigenrays is the more important.

## 4 CONCLUSIONS

Numerical prediction of bird vocalization propagation in the Alpine environment has been investigated. For this, a ray-tracing approach was chosen. While there are inherent limitations to geometrical acoustics (shadow zones and caustics), the model developed accounts for most of the physical phenomena encountered in sound propagation in a mountain environment. Outputs are narrow-band spectra as well-as waveforms, which could allow the analysis of bird vocalizations after propagation. Test-cases above a flat rigid ground have been done to validate the model. Finally, application of the model to predict the active space of rock ptarmigan has been illustrated and the feasibility of the approach has been demonstrated.

In future works, further analysis of the active spaces of rock ptarmigan will be done. In particular, influence of the meteorological conditions on the active spaces will be studied. The inverse problem that is determining for a given receiver the area on which rock ptarmigan can be detected will be investigated. Moreover, the study will be extended to other bird species.

## ACKNOWLEDGEMENTS

This work was performed within the framework of the Labex CeLyA of the Université de Lyon, within the programme 'Investissements d'Avenir' (ANR-10-LABX-0060/ANR-16-IDEX-0005) operated by the French National Research Agency (ANR).

## REFERENCES

- [1] Marin-Cudraz, T.; Muffat-Joly, B.; Novoa, C.; Aubry, P.; Desmet, J.-F., Mahamoud-Issa, M., Nicolè, F.; Van Niekerk, M.H.; Mathevon, N.; Sèbe, F. Acoustic monitoring of rock ptarmigan: A multi-year comparison with point-count protocol, *Ecological Indicators*, Vol 101, 2019, pp 710-719.
- [2] Marin-Cudraz, T.; Muffat-Joly, B.; Novoa, C.; Mathevon, N.; Sèbe, F. The use of bioacoustics to improve rock ptarmigan (*lagopus muta*) spring counts in the French Alps and Pyrenees, *Grouse News*, Vol 53, 2019, pp 23-28.
- [3] Rock ptarmigan. Wikipedia, [https://en.wikipedia.org/wiki/Rock\\_ptarmigan](https://en.wikipedia.org/wiki/Rock_ptarmigan) (Last viewed 5/29/2019).
- [4] Reed, S.E.; Boggs, J.L.; Mann, J.P. A GIS tool for modeling anthropogenic noise propagation in natural ecosystems, *Environmental Modelling & Software*, Vol 37, 2012, pp 1-5.
- [5] Candel, S. Numerical solution of conservation equations arising in linear wave theory: application to aeroacoustics, *Journal of Fluid Mechanics*, Vol 83 (5), 1977, pp 465-493.
- [6] Jensen, F.B.; Kuperman, W.A.; Porter, M.B.; Schmidt, H. *Computational ocean acoustics*, Springer, second edition, 2011.
- [7] Dragna, D.; Cotté, B.; Blanc-Benon, P.; Poisson, F. Time-domain simulations of outdoor sound propagation with suitable impedance boundary conditions, *AIAA Journal*, Vol 49 (7), 2011, pp 1420-1428.
- [8] Dragna, D.; Blanc-Benon, P.; Poisson, F. Time-domain solver in curvilinear coordinates for outdoor sound propagation over complex terrain, *Journal of the Acoustical Society of America*, Vol 113 (6), 2013, pp 3751-3763.